Research Article Vol. 31, No. 2 / 16 Jan 2023 / *Optics Express* 1354

Optics EXPRESS

Broadband polarization splitter-rotator on a thin-film lithium niobate with conversion-enhanced adiabatic tapers

YUAN SHEN,[1] ZILIANG RUAN,[2] KAIXUAN CHEN,[3] LIU LIU,[2] BIGENG CHEN,[1,*] AND YUNJIANG RAO[1,4]

[1] *Research Center for Optical Fiber Sensing, Zhejiang Laboratory, Hangzhou 310000, China*
[2] *State Key Laboratory for Modern Optical Instrumentation, College of Optical Science and Engineering, International Research Center for Advanced Photonics, Zhejiang University, Hangzhou 310058, China*
[3] *Guangdong Provincial Key Laboratory of Optical Information Materials and Technology, South China Academy of Advanced Optoelectronics, South China Normal University, Guangzhou 510006, China*
[4] *Fiber Optics Research Center (FORC), Key Lab of Optical Fiber Sensing and Communications, University of Electronic, Science and Technology of China, Chengdu 611731, China*
[*] *chenbg@zhejianglab.com*

Abstract: In this work, we propose and experimentally demonstrate a broadband polarization splitter-rotator (PSR) on the lithium niobate on insulator (LNOI). With multiple sequentially connected adiabatic tapers for waveguide mode conversion and directional coupling, the PSR shows a 160-nm bandwidth covering the C and L bands, an insertion loss of less than 2 dB, and an extinction ratio of more than 11 dB. Benefiting from the conversion-enhanced adiabatic tapers, the broadband device has a short length of 405 µm. Further optimization is performed to reduce the device length to 271 µm and comparable performances are achieved, demonstrating the feasibility of higher device compactness. The proposed design and principle can contribute to high-performance polarization management for integrated lithium niobate photonics.

1. Introduction

Thin-film lithium niobate on insulator (LNOI) has been considered one of the most promising integrated photonics platforms because of its multiple advantages such as low optical loss, linear electro-optical effect, and wide transparent window [1–3]. The existing LNOI nanofabrication techniques allow for optical modes and driving electric fields confined within the (sub)micrometer scale, and thus, orders of magnitude lower modulation voltages compared to conventional waveguide structures in bulky lithium niobate [4,5]. Consequently, high-speed LNOI photonic devices with COMS drivers have become feasible on chip, paving the way for highly integrated optoelectronic devices based on LNOI [6]. Similar to conventional approaches, wavelength division multiplexing (WDM) and polarization division multiplexing (PDM) [7] are direct methods for expanding the optical communication capacity using LNOI. WDM can directly benefit from the transparency that covers the visible and near-infrared regimes. For PDM, a polarization splitter-rotator (PSR) is essential at the receiver end to demultiplex the optical information encoded in two orthogonal polarizations. This functionality is also desired in on-chip optical quantum systems because polarization information is frequently used to distinguish quantum states [8]. From the viewpoint of system integration, an on-chip PSR [9] integrated with other devices monolithically can benefit from cost effectiveness, compactness, stability, etc. A few PSR designs based on LNOI, which use mode evolution sections to convert an input TM_0 mode to a TE_1 mode have recently been reported [10–12]. Subsequently, the TE_1 mode is converted to the TE_0 mode via asymmetrical directional coupling [10,11] or asymmetric Y-splitting [12]. However, mode evolution usually requires a long tapering waveguide (from a

#481652 https://doi.org/10.1364/OE.481652
Journal © 2023 Received 30 Nov 2022; revised 9 Dec 2022; accepted 10 Dec 2022; published 3 Jan 2023

few hundred μm to over 1 mm) to achieve ~100% conversion and support a large bandwidth simultaneously.

In this study, we propose a multi-taper design for LNOI-based PSRs to enhance mode conversions significantly. In the multi-taper structures, the direction of each taper is opposite to that of the adjacent tapers. The designed mode evolution section, as short as 82.2 μm, supports 99.8% conversion from the TM_0 mode to the TE_1 mode at a wavelength of 1550 nm in the simulation. To convert the TE_1 mode into a TE_0 mode, an asymmetrical directional coupler (ADC) was designed with the same multi-taper idea, realizing 99.7% conversion efficiency with a coupler length of only 90 μm. PSR devices consisting of the mode evolution and ADC sections were fabricated on an LNOI substrate. The measured transmission spectra showed that the operating bandwidth was as high as 160 nm. To the best of our knowledge, this is the largest experimentally obtained PSR bandwidth for LNOI reported to date. The actual bandwidth is expected to be larger but could not be fully revealed in the proof-of-concept measurement because of the limited wavelength ranges of the tunable laser and grating couplers (GCs). The entire device was only 405 μm long, including the two conversion sections, a transition waveguide, a TE_1-mode filter, and an S-bend of the ADC output. For the TM_0 input, the PSR insertion loss (IL) was less than 2 dB, and the extinction ratio (ER) was more than 11 dB. The TE_0 input demonstrates better performance with an IL of less than 1 dB and an ER greater than 22 dB. Further optimization of the ADC and S-bend realized a PSR device as short as 271 μm with comparable performance, making the PSR much more compact than those in previous experimental reports on LNOI [10–12]. The novel design concept with the proposed multi-taper structures for mode conversion was successfully validated in both simulations and experiments.

2. Structure design and simulation

The proposed PSR is based on 600-nm X-cut LNOI with the main propagation along the optical axis Z. As schematically shown in Fig. 1(a), it begins with a mode evolution section for converting an input TM_0 mode to a TE_1 mode. Then, the TE_1 mode is converted to a TE_0 mode using the following ADC section. We used an S-bend to guide the TE_0 mode to the cross port. An input TE_0 mode goes straight to the through port adiabatically without any conversion. A TE_1-stop filter using multi-mode interference (MMI) is added before the through port to suppress crosstalk from the TE_1 mode. The entire structure is formed by ridge waveguides (etched by 350 nm) and cladded by 1-μm SiO_2 (Fig. 1(b)). The sidewall angle is set to 60° according to our LNOI etching process. Our design features multi-taper structures, in which the direction of each taper is opposite to that of the adjacent tapers. These structures are applied in both the mode evolution and ADC sections for conversion enhancement, which will be explained theoretically in the following sections.

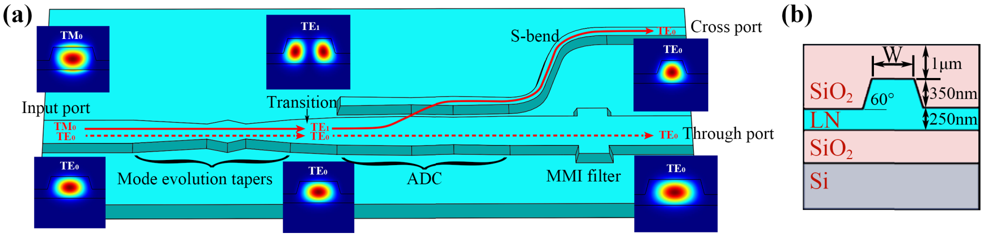

Fig. 1. (a) Schematic of the proposed PSR. (b) Cross-section of the LNOI ridge waveguide.

The broken vertical symmetry induced by the ridge waveguide and inclined sidewalls can lead to strong mode hybridization if the effective indices and mode profiles of the two waveguide modes are close to each other [13]. The waveguide structure is illustrated in Fig. 1(b). We calculated the effective indices of the first few modes in the LNOI waveguide versus the waveguide upper width using commercial software Lumerical Mode. The waveguide orientation is along the optical axis Z with an anisotropic refractive index described by the Sellmeier equation [14], where $n_o = 2.211$ and $n_e = 2.138$ at the wavelength of 1550 nm. It can be observed that the effective indices of the TM_0 and TE_1 modes become much closer in the width range of approximately 1.5-2.1 μm with an anti-crossing in the middle (Fig. 2(a)). At the anti-crossing, the difference in the mode indices is only 0.01. The TE polarization fractions (represented by the colors of the curves) suggest that the field intensity ratio of TE to TM for both modes approaches 50:50 around the anti-crossing. Therefore, we can expect similar mode profiles that facilitate mode hybridization. This is because the E_x and E_y profiles of the TM_0 and TE_1 modes are similar. When the TE-to-TM ratios of the two modes were close to 50:50, their composed magnitude profiles demonstrated the highest similarity. In this case, they can be easily hybridized and transferred to each other if sufficient perturbation is provided [13,15]. However , the polarization purity rapidly increases outside the range of 1.5-2.1 μm, leading to a significantly weaker mode hybridization. Hence, the taper end widths of the mode evolution section in our design are set to 1.5 μm and 2.1 μm.

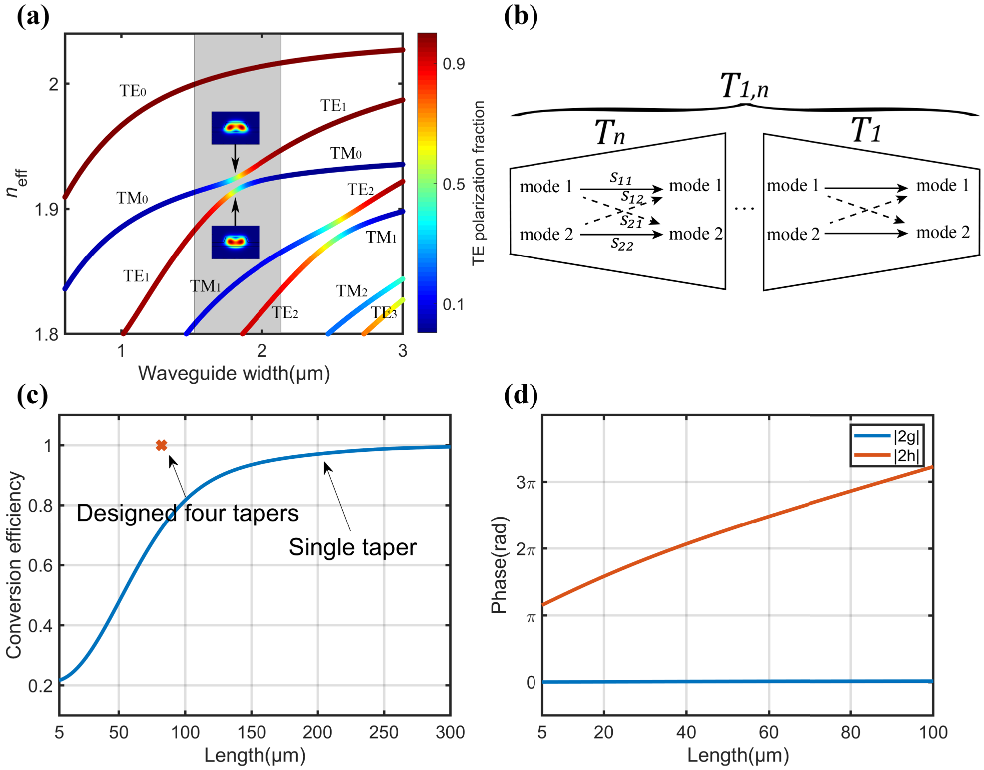

Fig. 2. (a) Effective indices of the first few modes supported by the LNOI waveguide dependent on the waveguide width at 1550 nm wavelength. The curve colors indicate the TE polarization fraction of the corresponding waveguide modes. Inset: Mode profiles of the TM_0 and TE_1 modes at the anti-crossing. (b) Mode conversion process in a multi-taper structure represented by the transmission matrix T_i with S-parameter elements. (c) Conversion efficiency of a single taper versus the taper length. The red mark indicates the conversion result of the proposed four-taper design. (d) Calculated phase differences $|2g|$ and $|2h|$ versus taper length.

A single waveguide taper is the simplest TM_0-TE_1 converter with a linearly varying width as a continuous perturbation. An S-parameter matrix [16] is used to describe the conversion process. Subsequently, the multi-taper conversion can be expressed as the product of the matrices for the tapers involved in order, as shown schematically in Fig. 2(b). The subscripts j and k ($j, k = 1, 2$) of matrix element s_{jk} denote the conversion from mode k to j. Consequently, the transmission matrix containing the amplitude and phase for any single taper can be expressed as

$$T = \begin{bmatrix} s_{11} & s_{12} \\ s_{21} & s_{22} \end{bmatrix} = \begin{bmatrix} \kappa_{11}\exp(ia_{11}) & \kappa_{12}\exp(ia_{12}) \\ \kappa_{21}\exp(ia_{21}) & \kappa_{22}\exp(ia_{22}) \end{bmatrix} \tag{1}$$

where i is an imaginary symbol and $\kappa_{jk}(j, k = 1, 2)$ is the conversion amplitude. Therefore, κ_{jk}^2 denotes the absolute conversion efficiency. The term $a_{jk}(j, k = 1, 2)$ is the phase change during conversion. Assuming that the transmission is lossless and the matrix is unitary, we can obtain $a_{11} + a_{22} = a_{12} + a_{21} + \pi$ and rewrite Eq. (1) for convenience as follows:

$$T = \exp(if)\begin{bmatrix} \cos r \exp(ig) & i\sin r \exp(ih) \\ i\sin r \exp(-ih) & \cos r \exp(-ig) \end{bmatrix} \tag{2}$$

where $\cos r = \kappa_{11} = \kappa_{22}$, $\sin r = \kappa_{12} = \kappa_{21}$, $f = (a_{11} + a_{22})/2$, $g = (a_{11} - a_{22})/2$ and $h = (a_{12} - a_{21})/2$. Therefore, r is defined as the angle of the conversion amplitude κ_{jk}. According to Eqs. (1) and (2), f is the phase change induced by light propagation, $2g$ is the phase difference induced by the different propagation constants of the two modes, and $2h$ is the difference between the phase changes of the two conversion processes, i.e., mode1→mode2 and mode2→mode1. For the two tapers connected end-to-end, the total transmission matrix can be simply expressed as

$$T_{1,2} = T_2 \cdot T_1 \tag{3}$$

where $T_{1,2}$ is the total transmission matrix for taper 1 (T_1) and taper 2 (T_2). It can be derived that the mode conversion efficiency $\sin^2 r_{1,2}$ satisfies the following relations:

$$\sin^2 r_{1,2} = \sin^2(r_1 + r_2)\cos^2\gamma + \sin^2(r_1 - r_2)\sin^2\gamma \tag{4}$$

where $\gamma = (g_1 - h_1)/2 + (g_2 + h_2)/2$. In the scenario studied in this work, it is straightforward to have

$$\sin^2 r_{1,2} = \sin^2(r_1 + r_2) - 4\sin r_1 \sin r_2 \cos r_1 \cos r_2 \sin^2\gamma \le \sin^2(r_1 + r_2) \tag{5}$$

$$\sin^2 r_{1,2} = \sin^2(r_1 - r_2) + 4\sin r_1 \sin r_2 \cos r_1 \cos r_2 \sin^2\gamma \ge \sin^2(r_1 - r_2) \tag{6}$$

Hence, we can obtain

$$|r_1 - r_2| \le r_{1,2} \le r_1 + r_2 \tag{7}$$

Specifically, $r_{1,2} = \pi/2(\sin^2 r_{1,2} = 1)$ only when $r_1 + r_2 = \pi/2$ and $\gamma = 0$. This relation can be readily extended to a general case with n transmission matrices. In the overall transmission matrix $T_{1,n} = \prod T_k$, $r_{1,n}$ follows the inequality

$$r_{1,n} \le r_{1,n-1} + r_n \le \cdots \le \sum_1^n r_k \tag{8}$$

Consequently, for an n-taper mode converter with a desired efficiency of 100% ($r_{1,n} = \pi/2$), the conversion amplitude angle conditions are

$$\begin{cases} r_1 + r_2 = \pi/2, & n = 2 \\ \sum_1^n r_k \ge \pi/2, & n \ge 3 \end{cases} \tag{9}$$

While the phase condition to achieve full conversion for the two-taper case is simply $\gamma = 0$, the general amplitude and phase conditions are more complicated with more taper parameters.

However, they can still be derived from the equation below using the cascading principle (similar to Eq. (4)):

$$\sin^2 r_{1,n} = \sin^2(r_{1,n-1} + r_n)\cos^2\gamma' + \sin^2(r_{1,n-1} - r_n)\sin^2\gamma' \tag{10}$$

where $\gamma' = (g_{1,n-1} - h_{1,n-1})/2 + (g_n + h_n)/2$.

The conversion efficiency of a single taper (width varying from 1.5 µm to 2.1 µm) versus the taper length was calculated using the eigen-mode expansion (EME) solver in Lumerical Mode, as shown in Fig. 2(c). Considering that nonadiabatic evolution may occur if the taper is too short, we calculated the efficiency from the 5-µm length. An efficiency of 99% requires a taper length of over 250 µm (Fig. 2(c)). This conversion process can be divided into two parts: fast (<120 µm) and slow (>120 µm). This phenomenon implies that there is an opportunity to reduce the total length requirement using multiple short tapers because each taper conversion can remain in the fast part. Simultaneously, the amplitude condition (Eq. (9)) given above can be fulfilled more easily. For the phase condition, straight waveguides may be employed to tune the phase between the tapers for a higher conversion efficiency [16] but an additional length is required. Here, we evaluate the phase information $|2g|$ and $|2h|$ of the single taper dependent on the length, as shown in Fig. 2(d). It can be observed that $|2g|$ remained nearly constant. This is because the average effective indices of the TM_0 and TE_1 modes are close to each other over the hybridization regime (gray region in Fig. 2(a)) and thus, the cumulative phase difference changes slightly. In contrast, $|2h|$ increases quickly with the taper length, which means that the shape parameter considerably affects the phase change during mode conversion. Notably, $|2h|$ changed by 2π when the length increased from 5 µm to 92 µm. These results suggest that the conversion amplitude and phase can be adjusted simultaneously and flexibly via single taper lengths in a multi-taper structure to realize ~100% conversion while shortening the total length.

Based on the derived theory, we propose a TM_0-TE_1 converter with four tapers to have sufficient degrees of freedom (lengths of the four tapers) for optimization and a reasonable computational resource load. As mentioned above, the taper end widths were set as 1.5 µm and 2.1 µm for the strongest mode hybridization. To avoid unwanted mode conversion during TM_0 propagation in the long access tapers between the GCs and PSR of the test device, the beginning and ending widths of the 4-taper mode evolution section (left part of Fig. 3(a)) are both set as 2.1 µm. Hence, accessing tapers with widths over 2.1 µm remains away from the hybridization regime. The four conversion tapers are then connected end-to-end in different directions. The particle swarm optimization method was used to simultaneously realize the maximum conversion and shortest total length. Consequently, we obtained a 99.8% conversion efficiency at a wavelength of 1550 nm with four tapers of lengths 38.9 µm, 10.8 µm, 9.3 µm, and 23.2 µm, respectively, resulting in a total length of only 82.2 µm (red mark in Fig. 2(c)). For a TE_0 input, the transmission is also as high as 99.8% in this structure according to our simulation results.

To separate the converted TE_1 mode and input TE_0 mode, a narrow branch waveguide is placed near the main waveguide to form an ADC (right part of Fig. 3(a)) that converts the TE_1 mode to a TE_0 mode. This TE_0 mode is then guided to the cross-port via the S-bend. This S-bend consists of two connected Euler bends with an 80-µm minimum radius at one end and an infinite curvature at the other end, resulting in a total S-bend length of 163 µm. When the effective index of the TE_1 mode in the main waveguide and that of the TE_0 mode in the branch waveguide are sufficiently close, directional coupling will be accompanied by the mode conversion simultaneously [10]. In contrast, the effective indices of the TE_0 modes in the main and branch waveguides have a sufficient difference (Δn=0.042) so that coupling can hardly occur between them. We observe that the starting part of the S-bend also contributes slightly to the coupling, which is considered when designing the ADC with the multi-taper idea. All geometrical parameters are shown in Fig. 3(a). The corresponding widths are maintained near the strongest mode coupling between the TE_1 and TE_0 modes, that is, approximately 2.5 µm for the main waveguides (TE_1) and approximately 0.99 µm for the branch waveguides (TE_0). Simulations were performed on a single-taper ADC and

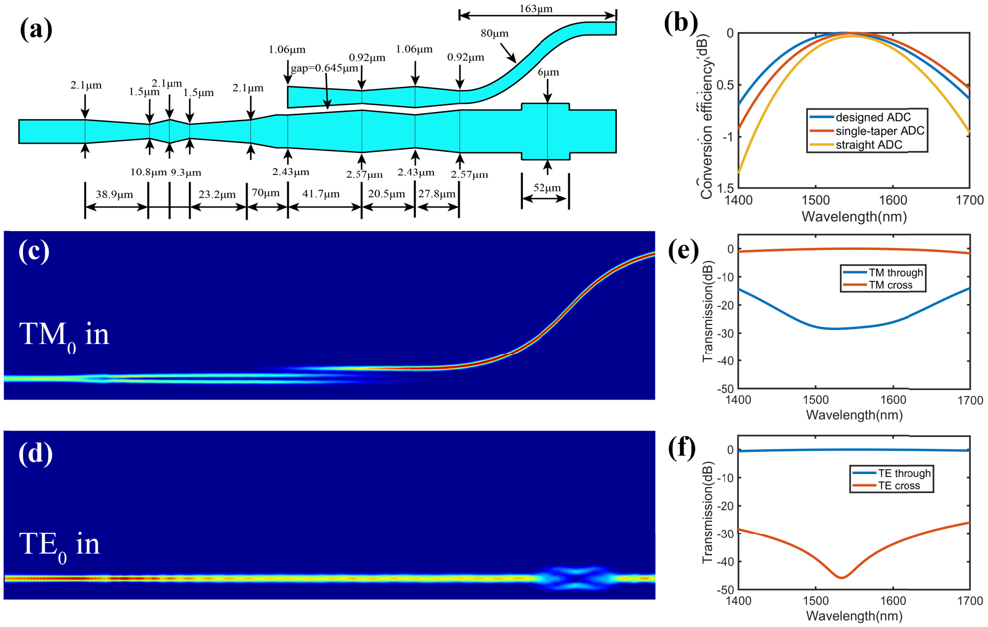

Fig. 3. (a) Schematic of the proposed PSR with detailed parameters. (b) Calculated TE_1-to-TE_0 conversion efficiencies of our proposed ADC (blue), single-taper ADC (red), and straight-waveguide ADC (yellow). (c, d) Simulated electric field magnitude distribution in the PSR at 1550 nm wavelength with TM_0 and TE_0 inputs, respectively. (e, f) Calculated transmission spectra of the PSR cross port and through port with TM_0 and TE_0 inputs, respectively.

straight-waveguide ADC for comparison. From the simulated conversion efficiencies, we observe that the single-taper and three-segmented ADCs have similar bandwidths, which are larger than that of the straight-waveguide ADC (Fig. 3(b)). The three-segmented ADC with 99.7% efficiency (1550 nm wavelength) was then adopted in the PSR device to verify the performance of the multi-taper design. Additionally, the input TE_0 mode can be effectively transmitted directly to the through port by the ADC with 99.9% transmission. The gap of the ADC is 0.645 μm, which can be easily realized using the existing nanofabrication process. A 1 × 1 filter is also employed to filter out the leaked TE_1 mode, which is not coupled to the S-bend. With the EME solver, the width is designed to be 6 μm and the length is 52 μm, making the TE_1-blocking efficiency at 1550 nm as high as 99%.

The electric field magnitude distributions of the entire PSR with TM_0 and TE_0 inputs at 1550 nm are shown in Fig. 3(c) and 3(d), respectively, which clearly demonstrate the polarization splitting and rotating functionality realized in the proposed structure. Remarkably, the simulated transmission spectra show that the PSR supports ultra-broadband operation, as depicted in Fig. 3(e) and 3(f). For the TM_0 input, the IL monitored at the cross port is less than 1.7 dB, whereas the ER is more than 12 dB in the wavelength range of 1400–1700 nm; For the TE_0 input, the IL monitored at the through port is less than 0.6 dB, whereas the ER is more than 26 dB in the same 300-nm range. These broadband characteristics can be attributed to the low dispersion of the LNOI waveguide structure. From 1400 nm to 1700 nm, the waveguide width corresponding to the anti-crossing point (Fig. 2(a)) only changes by approximately 10 nm, making the strong hybridization regime almost constant and supporting the broadband PSR design.

3. Fabrication and measurement

The proposed PSRs were fabricated on a 600-nm LNOI substrate with a 4.7-µm buried oxide layer. The substrate was patterned using electron beam lithography and then etched by 350 nm in depth with argon plasma-based reactive-ion etching, forming ridge waveguide structures with a 250-nm slab. A standard clean 1 (RCA 1) solution was used to remove the redeposition after etching. Finally, a 1-µm-thick SiO_2 upper cladding layer was deposited on the etched substrate. Fig. 4(a) shows the micrograph of the PSRs with TM and TE input GCs, respectively. The inset shows an enlarged image of the four-taper mode evolution section. For the TE GCs, the period was 0.89 µm, and the duty cycle was 0.304. For the TM GCs, the period was 1 µm, and the duty cycle was 0.236. The waveguide propagation loss of our LNOI platform was approximately 0.2 dB/cm obtained from a separate ring resonator measurement.

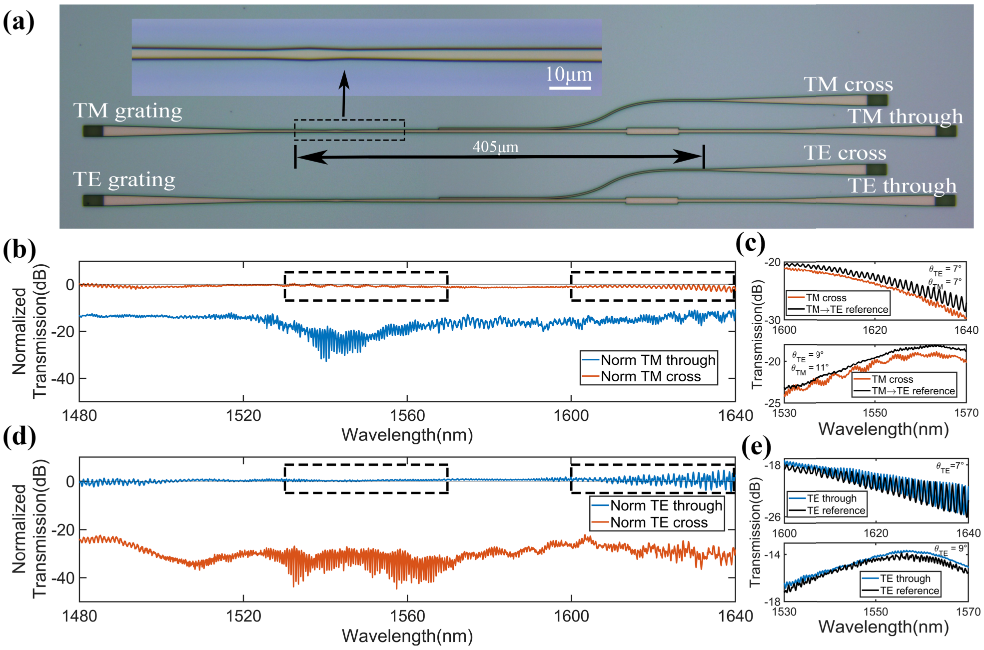

Fig. 4. (a) Micrograph of the fabricated PSRs. Inset shows a zoom-in picture of the four-taper mode evolution section. (b) Normalized transmission spectra of the cross port and through port with TM_0 inputs. (c) Raw transmission spectra of the measured cross port and reference with TM_0 inputs in two 40-nm wavelength ranges. θ refers to the inclined coupling fiber angle. (d) Normalized transmission spectra of the cross port and through port with TE_0 inputs. (e) Raw transmission spectra of the measured through port and reference with TE_0 inputs in two 40-nm wavelength ranges.

A continuous-wave tunable laser (Santec TSL-710, 1480-1640 nm) and a synchronized optical power meter (Santec MPM-210) were used to characterize the performance of the PSRs. The polarization of the input light was adjusted using a fiber polarization controller. With the TM-input PSR, the TM_0 IL is measured from the cross port (upper) and the ER is obtained by measuring the transmission ratio of the cross port to the through port; with the TE-input PSR, the TE_0 IL is measured from the through port, whereas the ER is obtained by measuring the transmission ratio of the through port to the cross port. Straight reference waveguides with TE and TM GCs were fabricated on the same chip for calibration. Each reference waveguide has two access tapers identical to those in the PSR device. The access tapers are connected by a 150-µm-long straight waveguide with negligible loss. Notably, all output GCs are TE GCs that can be directly used for the measurement of TM_0 IL (most TM_0 input light is converted to TE_0 light when coupled to the S-bend), TE_0 IL, and TE_0 ER. To obtain the TM_0 transmission from the TE output GC (through port) for the TM_0 ER, we used reference waveguides with TM GCs or TE GCs to perform the calibration. First, we maximize the transmission of the TM reference waveguide by adjusting the fiber polarization controller before the input fiber. Free-space polarizers were used to ensure the TM polarization purity. We then moved the fibers to couple with the TE reference waveguide as much as possible. The fiber angles were also optimized. By comparing the TM light transmission in the TM and TE reference waveguides, we obtained the amount of TM light before the TE output GC in the TM-input PSR for the TM ER figure.

We also noticed that the GCs had limited bandwidths (e.g., approximately 70 nm for a 3-dB decay in our TE GC) at certain fiber inclination angles. At wavelengths far away from the bandwidth, the weakly coupled light into the fibers is probably from a higher-order diffraction or scattering other than the first-order diffraction of the grating [17]. Consequently, using the result from a single full-range measurement as a reference or device transmission could lead to incorrect device transmission characteristics at wavelengths far from the GC bandwidth [18,19]. Therefore, we divided the full scanning range (160 nm) into several smaller ranges. The coupling of each range was optimized by adjusting the fiber angles and finely tuning the fiber alignment to the GCs [20]. For the TE GCs, we obtained the lowest GC loss of 7 dB at a 9° fiber angle and 1555-nm wavelength and the highest GC loss of 12 dB at an 11° fiber angle and 1485-nm wavelength. For the TM GCs, we obtained the lowest GC loss of 9 dB at an 11° fiber angle and 1580-nm wavelength and the highest GC loss of 14.5 dB at an 11° fiber angle and 1520-nm wavelength. To connect the separated transmission spectra correctly after normalization, the same range-splitting measurement was applied to both the PSR devices and reference waveguides with an identical fiber angle in each range.

Fig. 4(b) and 4(d) show the normalized transmission spectra from the cross ports (red) and through ports (blue) of the PSRs covering the full wavelength range (1480-1640 nm, C and L bands as well as part of the S band) with TM_0 and TE_0 inputs, respectively. These results are from the devices with −40 nm width bias compared with the optimized value in the simulation. This deviation may have been caused by fabrication errors. To demonstrate the reliability of the normalization, Figs. 4(c) shows the raw transmission spectra of the PSR cross port and the corresponding reference with TM_0 inputs in the 1600-1640 nm (upper panel) and 1530-1570 nm (lower panel) wavelength ranges. It should be noted that the TM→TE reference is a combination of the transmission spectra of the TE GC and TM GC. The reason for using this reference is that the input TM_0 mode was converted to the TE_0 mode at the cross-port of the PSR. Similarly, Fig. 4(e) shows the raw transmission spectra of the through port of the other PSR and the corresponding reference with TE_0 inputs in the same wavelength ranges. In this case, the reference spectrum is the transmission of the reference waveguide with two TE GCs.

The observed ripples in the transmission spectra can be attributed to the GC reflection back into the LNOI waveguides. This is because the fringe space matches the FSR of the presumed Fabry-Perot resonance in the PSR devices or reference waveguides with the GCs as reflectors at both ends. Specifically, strong ripples in the 1600-1640 nm (Fig. 4(d)) can be attributed to the different FSRs observed in the two raw transmission spectra (Fig. 4(e)). Because their envelopes corresponding to the actual device/reference transmissions are very close to each other, TE_0 IL can be regarded as <1 dB in this range. From 1480 nm to 1640 nm, the IL is approximately 2 dB, whereas the ER is more than 11 dB for the TM_0 input (Fig. 4(b)). For the TE_0 input, the normalized through transmission is slightly over 0 dB, which is mainly owing to the performance drift of the GCs between the reference waveguide and PSR device. Hence, we estimate that the IL for the TE_0 input is less than approximately 1 dB and the ER is more than 22 dB (Fig. 4(d)). Thus, we obtained an experimental PSR performance in qualitative agreement with our simulation results.

To determine the fabrication tolerance of the PSR, we measured the IL and ER depending on the waveguide width and ADC gap of the test devices, using a series of test devices with varying structural parameters. The step size between the adjacent width or gap variations was 40 nm. Fig. 5(a) and 5(b) show the measured TM_0-to-TE_0 conversion transmissions (cross) in the TM_0-input PSRs with varying widths and gaps, respectively, whereas Fig. 5(c) and 5(d) show the corresponding simulated transmissions. The structural parameters in the simulation were slightly adjusted to reflect the electron-beam lithography calibration result as much as possible, leading to performance shifts compared with those in Fig. 3(e). A wavelength range from 1530 nm to 1570 nm was chosen for the highest GC transmission. It can be observed that in the experiment, the transmission decreases from Δwidth=−40 nm (the result given in Fig. 3(b)) with increasing Δwidth, which agrees with the trend in the simulation although the maximum is at Δwidth=0 nm. We infer that the fabrication error is the main reason for this difference. For the varying ADC gap, the experiment also matches the simulation qualitatively because the transmission stays close at 0 nm or 40 nm but starts to decrease when Δgap exceeds this value. It can be concluded that an error of approximately ±40 nm for the width and gap is allowed for an excessive loss of 2 dB. Similarly, the width and gap error tolerances for the TM_0-to-TE_0 ER were also studied, as shown in Fig. 5(e)–5(h). The ER rapidly deteriorated as the width varied from the optimized value (Fig. 5(e) and 5(g)) but was relatively stable (Fig. 5(f) and 5(h)) with the varying gap. Because the ADC gap only affects the TE_1-to-TE_0 efficiency, whereas the residual TE_1 fraction is always blocked by the MMI filter, the residual TM_0 fraction to the through port is nearly uninfluenced by the gap. Therefore, we roughly estimated that the width tolerance for the 5-dB ER degradation was approximately ±20 nm according to the additional simulations with a smaller step, whereas the gap tolerance was over ±40 nm. Less tolerance was observed in the experimental results compared with the simulations. The IL and ER deteriorated faster in the fabricated devices when the studied parameters were biased from their optimized values. This will be left for further study because more parameters, such as the waveguide sidewall slope and actual rib height, could also contribute to this phenomenon.

The sidewall angle tolerance was also evaluated in simulation, as shown in Fig. 6. The TM_0 transmission monitored at the cross-port decreased by approximately 1 dB within the $\pm 4^\circ$ sidewall angle deviation (Fig. 6(a)) while the ER decreased from approximately 20 dB to 10 dB (Fig. 6(b)). Simultaneously, the ER changes were quite different for the positive and negative angle deviations. For a 5-dB ER degradation, the allowed sidewall angle deviation is from -1° to 2° approximately.

To evaluate the compactness potential of the device footprint, we attempted to optimize the S-bend and transition taper. The length of the Euler-type S-bend was reduced from 160 µm to 83.7 µm with a minimum radius of 60 µm while the transition was shortened from 70 µm to 10 µm. The length of the ADC was slightly optimized to 95.1 µm for maximum efficiency. Consequently, we obtained a total device length of 271 µm (Fig. 7(a)) that indicates a significantly higher compactness compared with the reported experimental LNOI PSRs. Fig. 7(b) shows the calculated transmission spectra of the full device with the TE_0 and TM_0 inputs, respectively. From the calculation results, we can infer that the broadband property of the PSR is well maintained by the optimized structural parameters. The measured normalized transmission spectra from the newly fabricated PSRs with the TM_0 and TE_0 inputs are shown in Figs. 7(c) and 7(d), respectively. We observed similar IL performances for both polarizations in the shorter PSRs except for the abnormal dips at approximately 1500 nm. This may be attributed to the cutoff of GCs which is more significant in the PSRs. Oscillating ripples are observed again in the longer wavelength range after 1600 nm, which are caused by the GC reflections. However, we observed that the ER performance is slightly worse than that of the 405-µm-long PSRs. This may be due to the dose drift of the electron beam lithography after a major maintenance. The dose drift can induce a

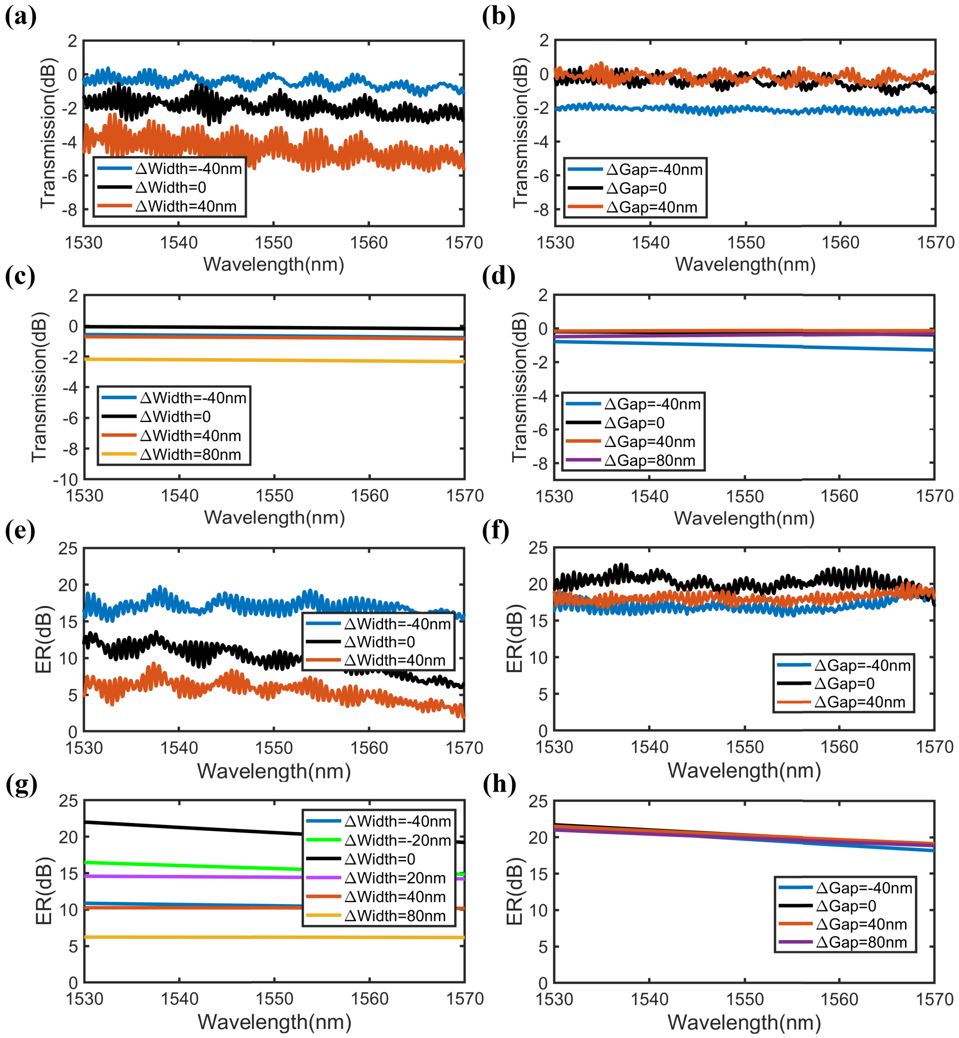

Fig. 5. (a-d) Measured and calculated transmission spectra of the cross port in the TM_0-input PSR with multiple width and gap variations, respectively. (e-h) Measured and calculated ER spectra of the TM_0-input PSR with multiple width and gap variations, respectively.

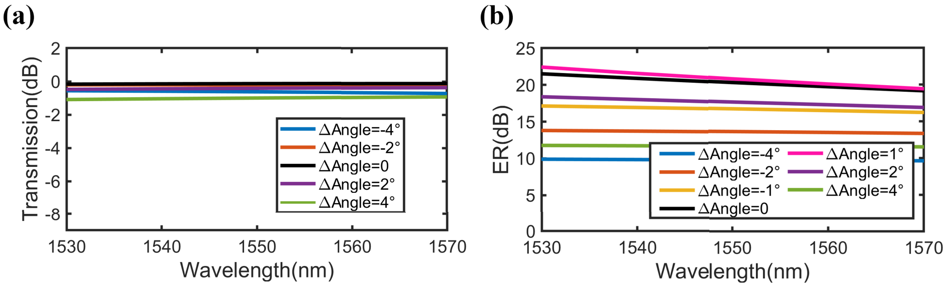

Fig. 6. (a, b) Calculated transmission and ER spectra of the TM_0-input PSR with multiple sidewall angle variations, respectively.

non-negligible waveguide width error, leading to incomplete TM_0-TE_1 conversion, as well as considerable TM_0 leakage to the through port (Fig. 5(g)).

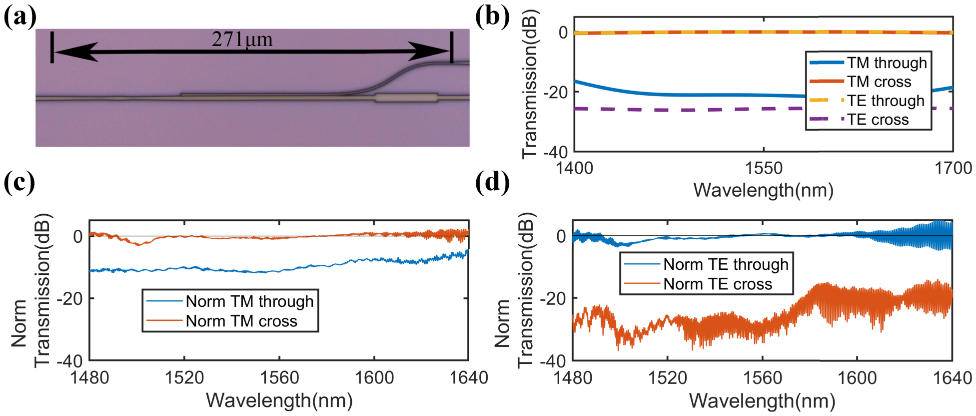

Fig. 7. (a) Micrograph of the shortened PSR. (b) Calculated transmission spectra of the full device with TM_0 and TE_0 inputs, respectively. (c) Normalized transmission spectra of the cross port and through port with TM_0 input. (d) Normalized transmission spectra of the cross port and through port with TE_0 input.

Table 1 summarizes several recent experimental studies of PSRs. Benefiting from the multi-taper idea, our design shows the largest bandwidth among the LNOI devices. The IL is competitive with other studies, and the ER is at an acceptable level. A few typical studies on silicon polarization splitters are also listed for comparison. While silicon has a high refractive index that is favorable for device compactness, lithium niobate with a much lower refractive index makes the PSRs one order of magnitude longer.

Table 1. Comparison of several recent experimental PSRs.

	IL (dB)	Bandwidth (nm)	ER (dB)	Device length(μm)
Taper with ADC[a] [10]	<2	130	>8	>7000
Taper with ADC[a] [11]	<0.65	>80 (O band)	20	431
Taper with Y-junction[a] [12]	<1	>60	>19.6	440
This work[a]	<2(TM_0) <1(TE_0)	160	>11(TM_0) >22(TE_0)	405
Taper with ADC[b] [9]	<1.5(TM_0) <0.5(TE_0)	90	>12(TM_0) >20(TE_0)	70
Dual etching[b] [21]	<1	150	>15	24
Sub-wavelength grating[b] [22]	<1(in 50 nm BW)	100	>15	35
Sub-wavelength grating[b] [23]	<1.4	120	>20	>151

[a] on LNOI platform
[b] on SOI platform

4. Conclusion

In this study, we demonstrated a broadband PSR on LNOI, which was inspired by the mode conversion in a multi-taper structure where each taper's direction is opposite to that of the adjacent ones. The theoretical conversion amplitude and phase conditions were rigorously derived using the S-parameter matrix method. We deduced that the amplitude and phase can be adjusted by each single taper length simultaneously and flexibly to achieve ~100% efficiency and a compact size. Based on this theory, we designed and fabricated PSRs with the multi-taper concept and realized a 160-nm operating bandwidth in a 405-μm-long device. In a wavelength range of 1480 nm to 1640 nm, the IL was less than 2 dB for the TM_0 input, and the corresponding ER was more than 11 dB; for the TE_0 input, the IL was less than 1 dB, and the ER was more than 22 dB. The fabrication tolerances were approximately ±40 for the 2-dB transmission degradation and approximately ±20nm for the 5-dB ER degradation. The critical dimension of the PSR was over 500 nm, which made it much easier to fabricate than the subwavelength grating structures [24]. Although the measurement range was limited by the tunable laser and GCs, the actual bandwidth of our PSR could be larger, as implied by our simulation and experimental results. The optimization of the transition taper and S-bend further reduced the total device length to 271 μm, indicating the compactness enhancement potential that exists in our design. Research involving PDM transmitters, polarization controllers, and other polarization-relevant LNOI devices could benefit from this study.

Funding. Center-initiated Research Project of Zhejiang Laboratory (K2022ME0AL04); Key Research Project of Zhejiang Laboratory (2020ME0AD02); National Natural Science Foundation of China (62105107, 62135012).

Disclosures. The authors declare that they have no conflicts of interest.

Data availability. The data underlying the results presented in this paper are not publicly available at this time but may be obtained from the authors upon reasonable request.

References

1. D. Zhu, L. Shao, M. Yu, R. Cheng, B. Desiatov, C. Xin, Y. Hu, J. Holzgrafe, S. Ghosh, A. Shams-Ansari, E. Puma, N. Sinclair, C. Reimer, M. Zhang, and M. Loncar, "Integrated photonics on thin-film lithium niobate," Adv. Opt. Photonics **13**(2), 242–352 (2021).
2. J. Lin, F. Bo, Y. Cheng, and J. Xu, "Advances in on-chip photonic devices based on lithium niobate on insulator," Photonics Res. **8**(12), 1910–1936 (2020).
3. Y. Qi and Y. Li, "Integrated lithium niobate photonics," Nanophotonics **9**(6), 1287–1320 (2020).
4. M. He, M. Xu, Y. Ren, J. Jian, Z. Ruan, Y. Xu, S. Gao, S. Sun, X. Wen, L. Zhou, L. Liu, C. Guo, H. Chen, S. Yu, L. Liu, and X. Cai, "High-performance hybrid silicon and lithium niobate Mach–Zehnder modulators for 100 Gbit s^{-1} and beyond," Nat. Photonics **13**(5), 359–364 (2019).
5. M. Xu, M. He, H. Zhang, J. Jian, Y. Pan, X. Liu, L. Chen, X. Meng, H. Chen, Z. Li, X. Xiao, S. Yu, S. Yu, and X. Cai, "High-performance coherent optical modulators based on thin-film lithium niobate platform," Nat. Commun. **11**(1), 1–7 (2020).
6. C. Wang, M. Zhang, X. Chen, M. Bertrand, A. Shams-Ansari, S. Chandrasekhar, P. Winzer, and M. Lončar, "Integrated lithium niobate electro-optic modulators operating at CMOS-compatible voltages," Nature **562**(7725), 101–104 (2018).
7. X. Chen, G. Raybon, D. Che, J. Cho, and K. Kim, "Transmission of 200-GBaud PDM probabilistically shaped 64-QAM signals modulated via a 100-GHz thin-film $LiNbO_3$ I/Q modulator," in *Optical Fiber Communication Conference*, (Optica Publishing Group, 2021), pp. F3C–5.
8. L. Feng, M. Zhang, Z. Zhou, M. Li, X. Xiong, L. Yu, B. Shi, G. Guo, D. Dai, X. Ren, and G. Guo, "On-chip coherent conversion of photonic quantum entanglement between different degrees of freedom," Nat. Commun. **7**(1), 11985 (2016).
9. D. Dai and H. Wu, "Realization of a compact polarization splitter-rotator on silicon," Opt. Lett. **41**(10), 2346–2349 (2016).
10. Z. Chen, J. Yang, W. Wong, E. Y. Pun, and C. Wang, "Broadband adiabatic polarization rotator-splitter based on a lithium niobate on insulator platform," Photonics Res. **9**(12), 2319–2324 (2021).
11. H. Luo, Z. Chen, H. Li, L. Chen, Y. Han, Z. Lin, S. Yu, and X. Cai, "High-performance polarization splitter-rotator based on lithium niobate-on-insulator platform," IEEE Photonics Technol. Lett. **33**(24), 1423–1426 (2021).
12. X. Wang, A. Pan, T. Li, C. Zeng, and J. Xia, "Efficient polarization splitter-rotator on thin-film lithium niobate," Opt. Express **29**(23), 38044–38052 (2021).
13. A. Kaushalram, G. Hegde, and S. Talabattula, "Mode hybridization analysis in thin film lithium niobate strip multimode waveguides," Sci. Rep. **10**(1), 16692 (2020).
14. D. E. Zelmon, D. L. Small, and D. Jundt, "Infrared corrected Sellmeier coefficients for congruently grown lithium niobate and 5 mol.% magnesium oxide–doped lithium niobate," J. Opt. Soc. Am. B **14**(12), 3319–3322 (1997).
15. G. Yang, A. V. Sergienko, and A. Ndao, "Tunable polarization mode conversion using thin-film lithium niobate ridge waveguide," Opt. Express **29**(12), 18565–18571 (2021).
16. J. Guo and Y. Zhao, "Analysis of mode hybridization in tapered waveguides," IEEE Photonics Technol. Lett. **27**(23), 2441–2444 (2015).
17. D. Taillaert, F. Van Laere, M. Ayre, W. Bogaerts, D. Van Thourhout, P. Bienstman, and R. Baets, "Grating couplers for coupling between optical fibers and nanophotonic waveguides," Jpn. J. Appl. Phys. **45**(8A), 6071–6077 (2006).

18. J. Ge, A. E. James, L. Xu, Y. Chen, K.-W. Kwok, and M. P. Fok, "Bidirectional soft silicone curvature sensor based on off-centered embedded fiber bragg grating," IEEE Photonics Technol. Lett. **28**(20), 2237–2240 (2016).
19. D. Liu, J. He, Y. Xiang, Y. Xu, and D. Dai, "High-performance silicon photonic filters based on all-passive tenth-order adiabatic elliptical-microrings," APL Photonics **7**(5), 051303 (2022).
20. H. Xu, D. Dai, and Y. Shi, "Ultra-broadband and ultra-compact on-chip silicon polarization beam splitter by using hetero-anisotropic metamaterials," Laser Photonics Rev. **13**(4), 1800349 (2019).
21. C. Xie, X. Zou, P. Li, L. Yan, and W. Pan, "Ultracompact silicon polarization splitter-rotator using a dual-etched and tapered coupler," Appl. Opt. **59**(30), 9540–9547 (2020).
22. M. Hou, Y. Wang, S. Liu, Z. Li, and P. Lu, "Multi-components interferometer based on partially filled dual-core photonic crystal fiber for temperature and strain sensing," IEEE Sens. J. **16**(16), 6192–6196 (2016).
23. M. Ma, A. H. Park, Y. Wang, H. Shoman, F. Zhang, N. A. Jaeger, and L. Chrostowski, "Sub-wavelength grating-assisted polarization splitter-rotators for silicon-on-insulator platforms," Opt. Express **27**(13), 17581–17591 (2019).
24. C. Deng, M. Lu, Y. Sun, L. Huang, D. Wang, G. Hu, R. Zhang, B. Yun, and Y. Cui, "Broadband and compact polarization beam splitter in LNOI hetero-anisotropic metamaterials," Opt. Express **29**(8), 11627–11634 (2021).